Small

NANO · MICRO small
www.small-journal.com

RESEARCH ARTICLE OPEN ACCESS

Inter-Crystal Spacing of Implantable Polymeric Surfaces as a Key Suppressor of Microbial Adhesion.

Kang Suk Lee[1,4] | Yohan Kim[1] | Jueun Kim[1,2] | Sungwoo Cho[1] | Dae-Hyun Kim[3] | Hak-Joon Sung[1,2,4]

[1]Department of Medical Engineering, Yonsei University College of Medicine, Seoul, Republic of Korea | [2]Department of Brain Korea 21 FOUR Project for Medical Science, Yonsei University College of Medicine, Seoul, Republic of Korea | [3]Department of Veterinary Surgery, College of Veterinary Medicine, Chungnam National University, Daejeon, Republic of Korea | [4]TMD LAB Co. Ltd., Seoul, Republic of Korea

Correspondence: Dae-Hyun Kim (vet1982@cnu.ac.kr) | Hak-Joon Sung (hj72sung@yuhs.ac)

Received: 6 August 2025 | **Revised:** 27 February 2026 | **Accepted:** 3 March 2026

Keywords: anti-biofilm | bacterial adhesion | polymer implant | semi-crystalline surface | shape memory polymer

ABSTRACT

Biofilm formation remains an ongoing challenge for implantable medical devices due to infection, drug resistance, and related complications. The device surface serves as the first line of defense against bacterial adhesion. Semi-crystalline polymers present repellent crystalline phases and attachable amorphous phases on their surfaces. Here, this intrinsic property is utilized to demonstrate an anti-biofilm mechanism by controlling the inter-crystal spacing in two cross-checkable types of shape memory polymer (SMP). When shape recovery is repeated (No → Once → Multiple: 10 times) through programming, the applied force and temperature fluctuation promote crystal alignment and growth on the polymer surface, accompanied by a reduction in amorphous spacing. Three representative biofilm-inducible bacterial species are cultured on the SMP surfaces. As the recovery cycle is repeated, progressive alignment and growth of the crystalline phase enhance bacterial repellency in collaboration with the reduction of amorphous space. When an SMP tube is used to replace a segment of the bile duct for 1 year in a dog model, biliary function is well maintained without biofilm formation or stenotic response through this mechanism. These results suggest a promising strategy for polymeric devices to amplify anti-biofilm effects under implantation by utilizing dynamic body movements as a driving force to align and grow crystalline phases.

1 | Introduction

Biofilm formation on implanted medical devices causes infection, drug resistance, and device failure. The resulting need for re-implantation and re-surgery places an increasing burden on patients [1–9]. As an initiating step of biofilm formation, bacteria attach to device surfaces and proliferate to form colonies accompanied by polysaccharide accumulation, which constructs a protective matrix in which bacteria reside. These polysaccharide matrices function as nutrient reservoirs and protective barriers against antibiotics. Once biofilm formation progresses, its removal becomes increasingly difficult, indicating that suppression of bacterial attachment and adhesion is the most effective strategy to prevent biofilm formation [10–16].

The surface of a device material serves as the primary landing site for bacteria and can therefore be regarded as the first-line defense against bacterial attachment and adhesion. Accordingly, extensive efforts have focused on modifying material surfaces to reduce biofilm formation, including antimicrobial coatings, anti-adhesive surface modifications, and drug-eluting functions [17–24]. As specific examples, zwitterionic polymer brushes

Kang Suk Lee, Yohan Kim, and Jueun Kim contributed equally to this work.

create inert surfaces via dense hydration layers [25], and antibiotic or silver nanoparticle composite coatings [26] provide anti-effects. Although these methods are promising to explore further in implantation conditions, long-term stability with sustainable performance should be improved further. Despite experimental success, surface degradation, delamination, erosion, and drug exhaustion limit clinical translation [27, 28]. Furthermore, these limitations become unpredictable and progressively deteriorative under dynamic implantation conditions, including movement, pH variation, inflammation, enzymatic reactions, protein adsorption, and cell-mediated remodeling. These challenges suggest that the material surface itself should inherently suppress bacterial attachment without reliance on coatings or additional modifications, and that the anti-bacterial surface property should be preserved or even strengthened over time during implantation.

Device materials are generally classified as crystalline or non-crystalline, with metals, ceramics, and polymers representing the three major categories [29–31]. Polymers typically exhibit both crystalline and amorphous phases due to their semi-crystalline nature, in contrast to the predominantly crystalline structures of metals and ceramics, with some exceptions (e.g., glass). In surface crystalline phases, the tight packing of polymer chains limits water penetration, thereby suppressing protein adsorption and subsequent cell adhesion, unlike the loosely packed amorphous phases [22, 32–35]. Crystalline phases can undergo growth, size modulation, and alignment in response to temperature changes. Directional forces and temperature fluctuations tend to stimulate crystalline growth and alignment. This behavior introduces an underexplored opportunity to continuously strengthen the anti-biofilm effect of device surfaces at implantation sites. Bodily movement induces directional stress propagation, and on-and-off interactions with intrabody fluid flow dynamically alter the local temperature, providing intrinsic stimuli for surface reorganization.

Bacteria attach to amorphous phases following protein adsorption, and the amorphous phase space is reduced upon crystalline growth with incremental alignment [36–39]. The size of bacteria usually ranges from 0.5–5μm, suggesting that reduction of amorphous space to the size range of bacteria is a key conceptual strategy to suppress bacterial attachment. Shape memory polymers represent a reliable model to control crystalline behavior and amorphous spacing using a programmable setup. Shape programming requires a temperature shift to induce a mobile state of polymer chains, followed by application of directional forces to change the shape from an original to a temporary configuration. The temporary shape is then fixed by cooling and maintained until gradual temperature increase triggers shape recovery by re-mobilizing polymer chains [40–42]. Although previous studies have shown promising reductions in biofilm formation upon repetition of shape recovery [43, 44], elucidation of the polymer surface properties responsible for bacterial repellency would enable broader application to other implantable polymeric devices. During the programming process, temperature fluctuation and directional force promote crystalline alignment and growth, which increase with repeated recovery cycles. As mechanistic contributors, this study proposes that these crystalline dynamics directly regulate the anti-biofilm function of polymer surfaces.

This study scrutinizes the following main subjects. i) Crystalline alignment with growth can reduce the counterpart amorphous (inter-crystal) spacing down to bacterial sizes. ii) This crystalline behavior can be controlled by directional forces with temperature fluctuation. iii) The reduction of inter-crystal spacing can serve as a key mechanism to suppress bacterial attachment (Figure 1a). Two cross-checkable types of shape memory polymer (SMP) are used as a simulative model of surface phase responsiveness to directional force and temperature changes under implantation in the body. When the recovery cycle is repeated (No → Once → Multiple: 10 times), the corresponding behaviors of crystalline (growth and alignment) and amorphous (space reduction) phases are validated by characterizing a series of thermal and surface properties. Three representative types of biofilm-inducible bacteria, including *Escherichia coli (E. Coli), Pseudomonas aeruginosa (P. aeruginosa)*, and *Staphylococcus aureus (S. aureus)*, are cultured onto test SMP types for 36 h. Their incremental detachment from the SMP surfaces is subsequently examined as the shape recovery is repeated. The bile duct is considered an organ with frequent biofilm formation upon stenting. Thus, as a harsh model to induce biofilm formation, a segment of the canine bile duct is replaced by an SMP tube with a venous wrap for 1 year. Patency management, histology, and phase behavior are then examined to validate the mechanistic effect in vivo over a long period. The results provide a foundational concept for utilizing the semi-crystalline nature of polymers to endow device surfaces with anti-biofilm properties under implantation. In particular, generic factors present at implantation sites, including movement and temperature fluctuation, are leveraged to strengthen the mechanism over time. As a key contribution, this concept offers a cornerstone for opening a new avenue toward next-generation anti-bacterial implantable devices.

2 | Results

2.1 | Effects of Repeated Shape Programing on Inter-Crystal Spacing

As a model to control inter-crystal spacing under directional force and temperature fluctuation, polycaprolactone (PCL)-based SMP (C-SMP) is synthesized through a double ring-opening polymerization of ε-caprolactone (CL) and glycidyl methacrylate (GMA) (Figure S1a) [45–49]. As another cross-checkable model, polylactic acid (PLA)-based SMP (L-SMP) is synthesized through a graft reaction of PLA and PCL using benzoyl peroxide (BPO) (Figure S1b). C-SMP and L-SMP undergo shape recovery at temperatures corresponding to melting (T_m) and glass transition (T_g), respectively. In differential scanning calorimetry (DSC) analyses, C-SMP exhibits a reduction of melting temperature (T_m) to the body temperature range (37.9°C) after ultra-violet (UV) crosslinking, indicating reduced crystallinity (Figure S1c). Likewise, the T_g of L-SMP is reduced to 36.6°C compared to that of PLA (Figure S1d). In cooling scans, the crystallization temperature (T_c) of C-SMP (Figure S1e) increases from Original to Recovery (multiple) upon crystallization. In contrast to the semi-crystalline PCL-dominant C-SMP, L-SMP does not exhibit T_c because amorphous PLLA is dominant in the composition. These results indicate that both SMP types can recover the original shape from the temporary one upon implantation into the body, as demonstrated (Figure S1f).

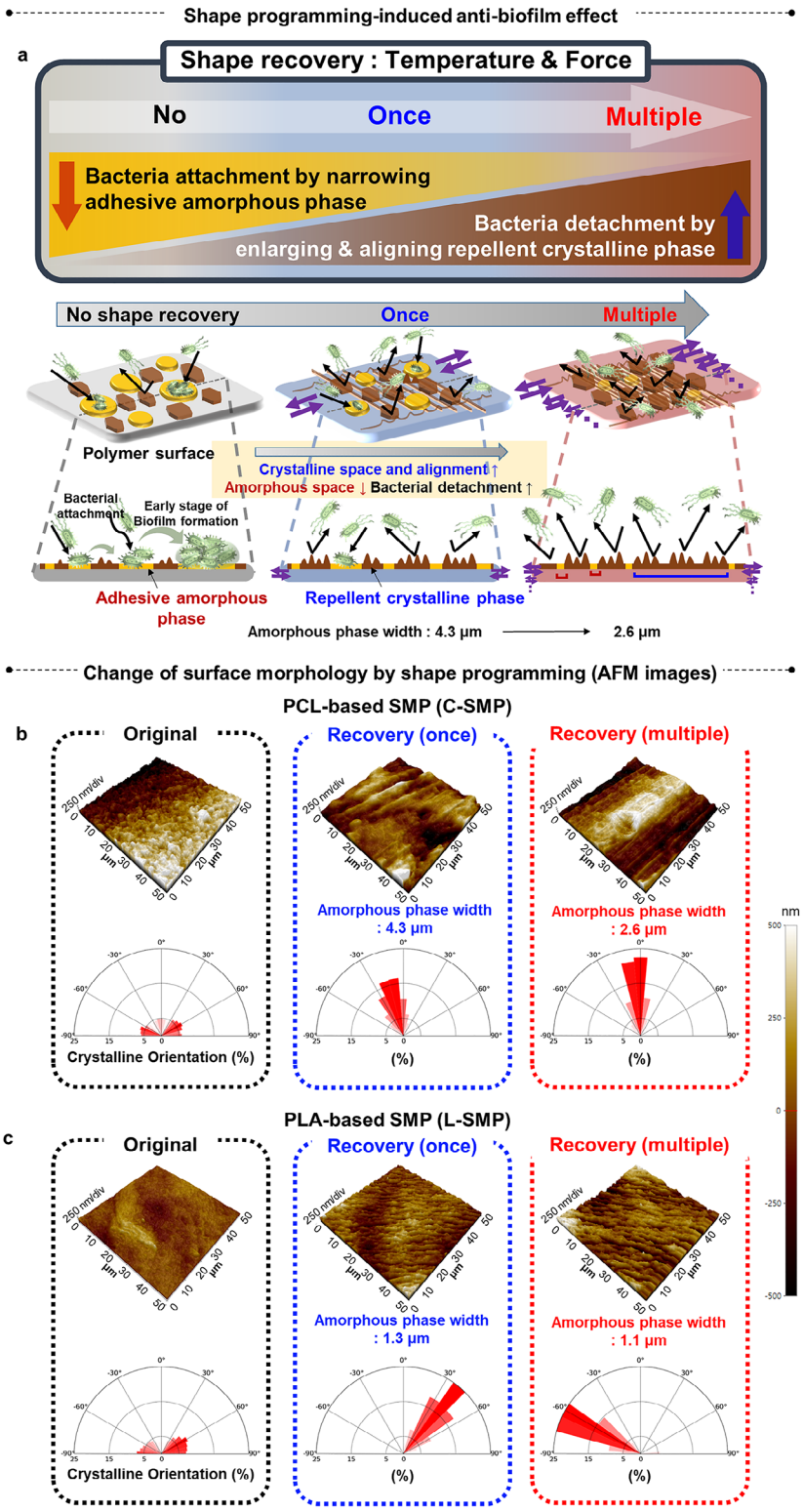

FIGURE 1 | Shape programming-induced anti-biofilm effect by inter-crystal spacing control. (a), Shape memory polymer (SMP) serves as a model to control inter-crystal spacing because the crystalline and amorphous phases undergo dynamic changes through programming between original and temporary shapes. When the shape recovery is repeated (No → Once → Multiple: 10 times), the applied force and temperature fluctuation promote crystal alignment and growth on the polymer surface along with a reduction of amorphous spaces. In this way, bacterial detachment by the repellent crystalline phase increases in collaboration with reduced bacterial attachment onto the amorphous space, thereby amplifying the anti-biofilm effect. (b–c), Analysis of AFM images shows that repetition of shape recovery reduces the amorphous width (groove pitch) while promoting crystalline orientation from once to multiple programming with denser packing in both PCL-based SMP (C-SMP: top) and PLA-SMP (L-SMP: bottom). Notably, repetition of shape recovery decreases the amorphous width of C-SMP from 4.3 to 2.6 μm, corresponding to a reduction from 1.3 to 1.1 μm in L-SMP.

Shape programming of these SMPs is carried out in film form by first deforming the original shape (film) into a temporary shape through stretching under 100% strain at the T_m or T_g of each SMP, with a further increase of 15°C (Figure 1a). The stretched films are fixed at −80°C, followed by restoration to the original film shape by heating to the T_m or T_g. When the shape recovery is repeated (No → Once → Multiple: 10 times) through programming, the applied force and temperature fluctuation promote crystalline alignment and growth of the polymer surface along with a reduction in amorphous spaces. In this way, bacterial detachment by the repellent crystalline phase increases in collaboration with reduced bacterial attachment onto the amorphous regions, thereby amplifying the anti-biofilm effect. Analysis of atomic force microscopy (AFM) images (Figure 1b,c) shows crystalline phases as bright protrusions and ridges, in contrast to dark amorphous grounds and valleys. Repeated shape recovery reduces the amorphous width (groove pitch) while promoting crystalline orientation from once to multiple programming, resulting in denser packing in both C-SMP and L-SMP. Notably, repeated shape recovery decreases the amorphous width of C-SMP from 4.3 to 2.6 μm, corresponding to a reduction from 1.3 to 1.1 μm in L-SMP. These results suggest that repeated shape programming promotes alignment and expansion of crystalline phases with a concomitant reduction of amorphous spacing.

2.2 | In Vitro Validation of Anti-Biofilm Effect by Repetition of Shape Programin

Biofilm formation in the body is initiated by bacteria adhesion. The major representative species include *E. coli, P. aeruginosa*, and *S. aureus* with typical dimensions of 1-2 × 0.5 μm (*E. coli*), 1 × 0.5 μm (*P. aeruginosa*), and 0.5–1.5 μm (*S. aureus*) [50, 51]. The experiments were independently repeated three times per condition (n = 3) by culturing identical bacterial concentrations, and the results were statistically analyzed to account for variations among individual samples. Although the dimensions of individual bacteria generally range from 0.5 to 2 μm, their adhesion is stabilized through the formation of microcolonies consisting of tens to thousands of bacteria (>5μm), which represents a strategic target for suppressing biofilm formation by reducing the amorphous phase. Accordingly, it is hypothesized that while single bacteria can initially attach to amorphous phases, subsequent colony formation is increasingly restricted as the programming cycle is repeated due to progressive reduction of amorphous spacing, resulting in detachment during microcolony development [52–54]. These Gram-positive (*S. aureus*) and Gram-negative (*E. coli* and *P. aeruginosa*) bacteria are cultured on the test SMP surfaces for 36 h (Figure 2). Samples are stained with crystal violet and bacteria-specific fluorescent probes to quantitatively analyze biofilm formation, providing dual quantitative validation of bacterial adhesion and accumulation [55–57].

The repetition of C-SMP programming up to 10 times significantly reduces the biofilm components regardless of bacterial type by at least 78% (Figure 2a), indicating an incremental anti-biofilm effect with repeated recovery cycles. These results are further validated by a decrease in bacterial number of at least 65% based on fluorescence staining analysis (Figure 2b). Repetition of L-SMP programming up to 10 times shows a similar trend, significantly suppressing biofilm formation by at least 62% according to quantitative crystal violet staining (Figure 2c). This outcome is supported by a 25 to 43% reduction in bacterial number based on fluorescence staining analysis (Figure 2d). Although biofilm formation on L-SMP is not significantly reduced from no to once recovery cycle by fluorescence analysis, a significant reduction is observed from no to multiple recovery cycles. Together with the results of crystal violet analysis, the overall statistical trends across three bacterial strains indicate clear reductions in biofilm formation on L-SMP. The reduction of colony formation on both SMP surfaces correlates with the reduction of amorphous spacing resulting from crystalline growth and alignment following repeated recovery cycles.

As a visible confirmation, repetition of C-SMP programming substantially reduces both the number and colony size of each bacterial type under fluorescence imaging with DAPI (4',6-Diamidino-2-phenylindole) DNA staining (Figure 2e; Figure S2a,b) [58, 59]. In addition, attachment of *E. coli* (blue, DAPI) and adsorption of fibronectin (green, FITC) onto amorphous spaces of C-SMP are examined under fluorescence microscopy (Figure S3a), followed by identification of crystalline phases using polarized optical microscopy (Figure S3b). Overlay of the two microscopy techniques reveals that bacteria preferentially attach to amorphous spaces with strong fibronectin adsorption signals located between crystalline ridges. These features indicate a causative role of protein adsorption onto amorphous spaces in bacterial adhesion. As the recovery cycle increases (No → Once → Multiple: 10 times), both fluorescence signals decrease markedly. This observation is further supported by a significant decrease in fibronectin adsorption on the film surface from no to multiple programming cycles, accompanied by a corresponding increase of residual protein in the supernatant (Figure S3c). This result is confirmed by albumin adsorption on the film surface (Figure S3d).

Real-time monitoring (Movies S1–S3) reveals that bacterial colony size decreases with increasing recovery cycles. Moreover, directional bacterial movement is observed, appearing to follow the orientation of amorphous pathways formed by crystalline alignment, as indicated by increased directional motion with repeated shape recovery. This behavior is further confirmed by triggering shape recovery near body temperature under real-time monitoring (Movie S4). Before shape recovery, bacteria are distributed randomly across the SMP surface. Upon returning to the original shape, bacteria begin to move in a directional manner, corresponding to increased phase alignment on the polymer surface.

2.3 | Crystalline Growth to Merge and Align Narrowing Amorphous Spaces Following Recovery Cycles

Semi-crystalline polymers such as PCL consist of amorphous regions and crystalline regions that are randomly distributed within the polymer matrix [60, 61]. Repetition of shape recovery (No → Once → Multiple: 10 times) increases the alignment of repellent crystalline phases along with their growth, thereby reducing the attachable amorphous space (Figure 3a), which acts as a key suppressor of biofilm formation. In DSC analyses, the T_m of C-SMP increases from 37.35°C to 39.09°C after 10 repetitions of

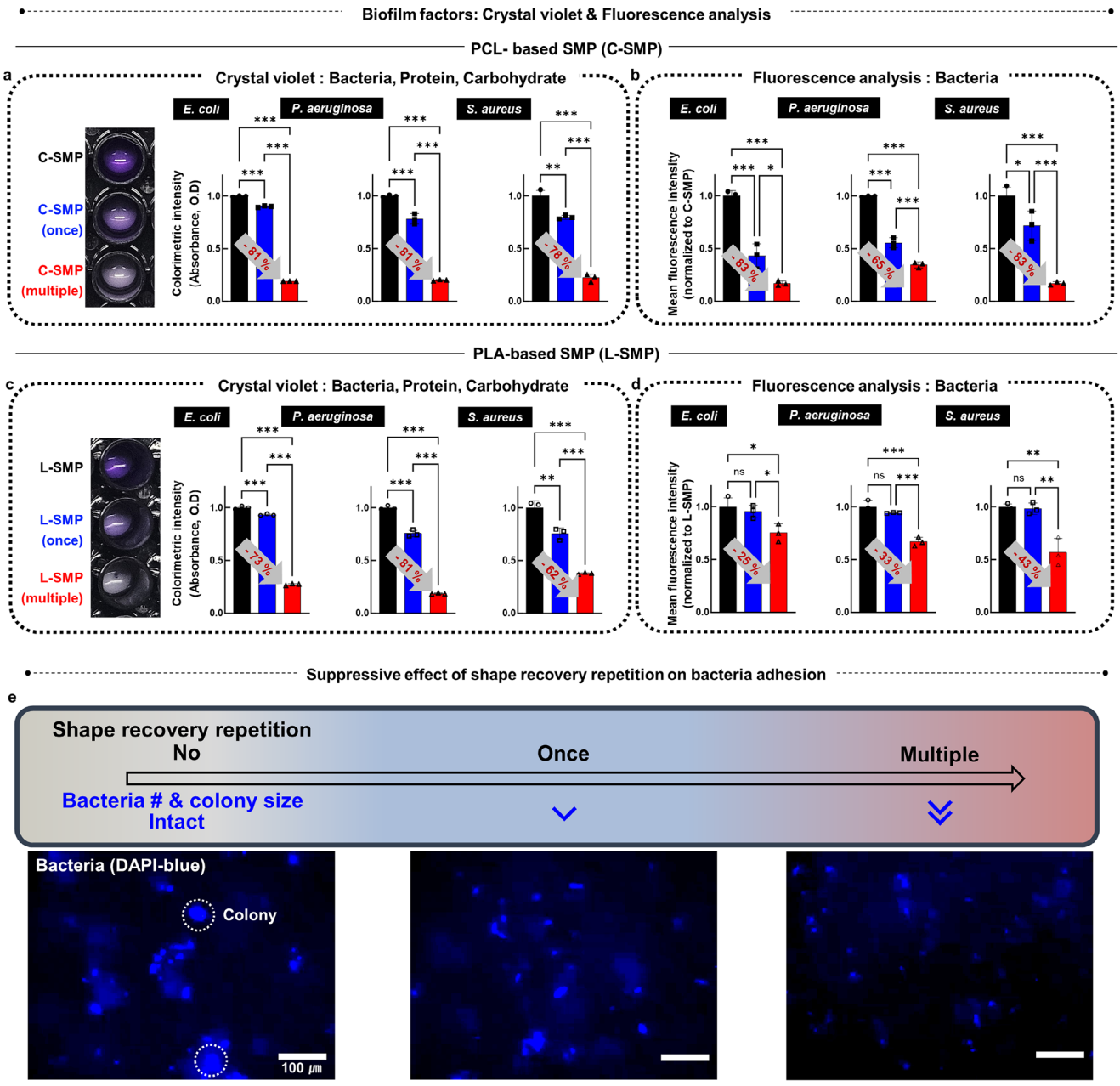

FIGURE 2 | In vitro validation of anti-biofilm effect by repetition of shape programing. Representative biofilm-inducible bacteria (*E. coli*, *P. aeruginosa*, and *S. aureus*) are cultured on the two SMP types for 36 h. Samples are stained with crystal violet and bacteria-specific fluorescence staining to quantitatively analyze the biofilm components as double quantitative validation. (a), Representative images show crystal violet staining of *E. coli* culture on C-SMP. Repetition of C-SMP programing up to 10 times significantly reduces the biofilm components by at least 78%, regardless of bacterial type, indicating an incremental anti-biofilm effect induced by repetition. (b), These results are further validated by a reduction in bacterial number of at least 65% based on fluorescent staining analysis. (c), Representative images show crystal violet staining of *E. coli* cultured on L-SMP. Repetition of L-SMP programing up to 10 times shows similar trends, suppressing biofilm formation significantly by at least 62% based on quantitative crystal violet analysis. (d), Fluorescent staining analysis shows a reduction in bacterial number ranging from 25% to 43%. (e), As a visible confirmation, repetition of C-SMP programing substantially reduces both bacterial number and colony size under fluorescence imaging with DAPI DNA staining. Data = mean ± SD (n = 3, NS: non-significant). *p < 0.05; **p < 0.01; ***p < 0.001 between the lined groups.

shape recovery (Figure 3b). This shift is attributed to an increase in crystallinity (χ_c) by 5.28% (Figure 3c). When wide-angle x-ray diffraction (WARD) patterns are analyzed, repetition of shape recovery generates a new peak at 21.9°, indicating the formation of a new crystalline domain in C-SMP (Figure 3d). As crystallite size is calculated using the Scherrer equation, the crystallite sizes at 21.3° and 23.6° increase by up to 11% following the recovery cycles (Figure 3e) [62, 63]. The newly observed peak at 21.9° corresponds to an intermediate crystallite size between those at 21.3° and 23.6°.

The T_g of L-SMP is within the body temperature range and increases by 2.6°C after 10 recovery cycles, as determined by DSC analyses (Figure 3f). This change is also driven by a 3.31% increase in χ_c (Figure 3g). The peaks at 12.4° and 14.7°

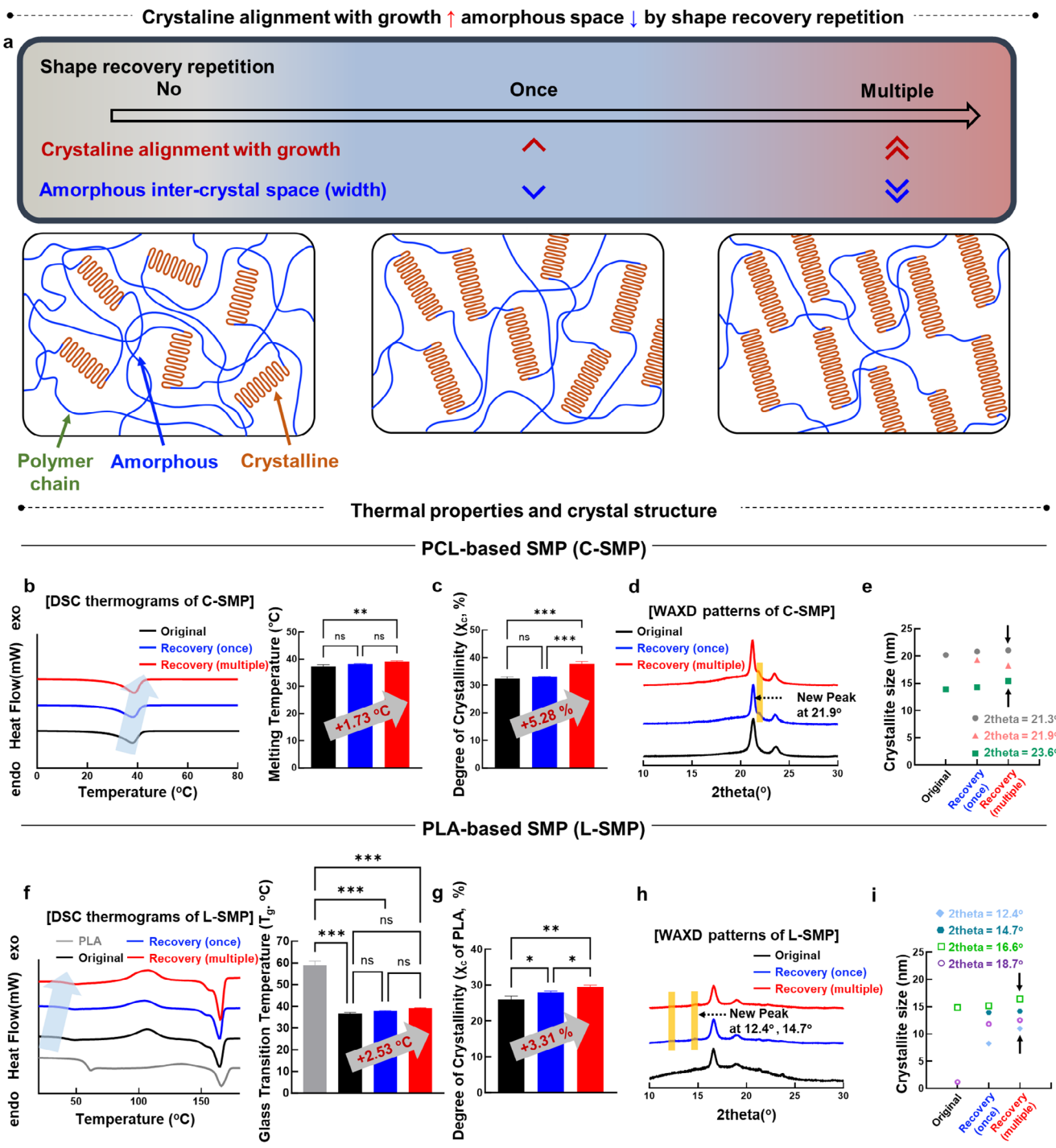

FIGURE 3 | Growing crystalline alignment to reduce amorphous spaces as key effectors of shape recovery repetition. (a), The repetition of shape recovery (No → Once → Multiple: 10 times) increases repellent crystalline alignment with growth, thereby reducing attachable amorphous spaces, which act as key suppressors of biofilm formation. (b), The melting temperature (T_m) of C-SMP increases from 37.35°C to 39.09°C after 10 repetitions of shape recovery in DSC, (c), which is attributed to an increase in crystallinity (χ_c) by 5.28%. (d), The repetition of shape recovery generates a new peak at 21.9°, indicating the formation of a new crystalline domain in C-SMP. (e), When the crystallite size is calculated using the Scherrer equation, the crystallite sizes at 21.3° and 23.6° increase by up to 11% following ten recovery cycles. The new peak (21.9°) indicates an intermediate crystallite size between those at 21.3° and 23.6°. (f), The glass transition temperature (T_g) of L-SMP is ranged around the body temperature and increases by 2.6°C along with 10 recovery cycles, (g), which is also driven by a 3.31% increase in χ_c. (h), The peaks at 12.4° and 14.7° indicate the formation of new crystalline domains in L-SMP. (i), The crystallite size increases following 10 recovery cycles, leading to tighter packing of the crystalline structure through rearrangement of polymer chains. Data = mean ± SD (n = 3, NS: non-significant). *p < 0.05; **p < 0.01; ***p < 0.001 between the lined groups.

indicate the formation of new crystalline domains in L-SMP, as shown by the WARD patterns (Figure 3h). The crystallite size increases following 10 recovery cycles, leading to tighter packing of the crystalline structure with rearrangement of polymer chains (Figure 3i). These results confirm that repetition of the shape memory process enhances the crystallinity with more ordered packing of polymer chains.

The structural changes and intermolecular interactions are examined during incremental crystallization of SMP following recovery cycles (No → Once → Multiple: 10 times) by analyzing carbonyl stretching (C═O) using Fourier-transform infrared (FT-IR) spectroscopy (Figure 4a–d). C-SMP exhibits newly grown crystalline-like areas (Green peak at 1696 cm^{-1}) accompanied by a reduction of amorphous areas (Blue peak at 1723 cm^{-1}), while maintaining the crystalline area (Red peak at 1747 cm^{-1}) in FT-IR spectra [64–66]. For L-SMP, the PCL (Green peak at 1720 cm^{-1}) and PLA (Violet peak at 1758 cm^{-1}) components are analyzed using FT-IR spectra (Figure 4e–h). While the PLA-associated area remains unchanged following recovery cycles, the generation of crystalline-like areas (Yellow peak at 1684 cm^{-1}) increases concurrently with a reduction of the PCL-associated area, indicating the recovery-induced crystallization of PCL accompanied by area loss [67, 68].

Surface energy is calculated from water contact angle measurements following recovery cycles (Figure 4i,j). Crystalline phases impede water penetration due to tight polymer chain packing, whereas ridge formation facilitates water infiltration into amorphous regions upon merging and alignment. This mechanism drives reductions in both amorphous width and water contact angle, accompanied by increases in crystallinity and surface energy following recovery cycles in both C-SMP and L-SMP [69, 70]. Moreover, proportional correlations are observed between surface energy and crystallinity with incremental trends, as well as between contact angle and amorphous width with decremental trends (Figure S4a). These results indicate cooperative surface effects of C-SMP and L-SMP that contribute to suppression of biofilm formation. Mechanical stress and heat fluctuation promote incremental crystalline growth when recovery cycles are repeated up to implantation-relevant conditions (in vivo) (Figure S4b). Consequently, surface roughness parameters (R_a and R_q) increase, reflecting enhanced height differences between crystalline ridges and amorphous regions. When the C-SMP surface is pressed or scratched using sandpaper (100 grit) in addition to glass pressing, patterning is generated without significant alteration of crystallinity (Figure S4c). As a result, the water contact angle decreases significantly, indicating a causative role of pattering in hydrophilicity.

It is generally understood that hydrophilic surfaces tend to hinder protein adsorption and subsequent cell adhesion compared to hydrophobic surfaces [7, 16, 71]. When this general principle is considered together with the observed increase in surface energy, the formation of crystalline ridges through growth and alignment, accompanied by merging and narrowing of amorphous spaces, appears to play a major role in reducing bacterial adhesion. The effect of narrowing amorphous spacing on bacterial detachment is further strengthened by the formation of highly aligned crystalline ridges. This is because the elevated ridges and the reduced landing sites act cooperatively as physical barriers to focal adhesion formation across the crystalline and amorphous phases, thereby promoting bacterial detachment.

2.4 | 1-Year Validation of In Vivo Anti-Biofilm Effect in Replacement of Canine Bile Duct

An autogenous saphenous vein (diameter: 2.0 mm, length: 30 mm) is harvested through a midline incision and implanted into the left bile duct of a Beagle dog. A C-SMP tube is fabricated with the same dimensions as the saphenous vein, followed by longitudinal stretching at the T_m to circumferentially reduce the diameter below 2.0 mm (temporary shape) upon cooling. As illustrated (Figure 5a), the tube is inserted into the vein and treated with 37°C saline so that the tube expands upon shape recovery to fit tightly inside the vein. This graft is used to replace a segment of the canine bile duct for 1 year, considering that biofilm formation typically occurs within 3 months post biliary stenting [2–6]. Biliary patency is well maintained for 1 year as examined by fluoroscopic cholangiography. When the bile duct is harvested after 1 year (Figure 5b), the H&E image (right) of the saphenous vein at the replaced position demonstrates maintenance of lining cells without any indication of stenosis around the surface of the C-SMP tube (sky blue), comparable to the normal vein (left). The C-SMP tube is not observed due to detachment from the vein during the staining process.

Blood analysis after 1 year using complete blood counts and biochemical panels confirms the absence of infection and preservation of bile duct function (Figure 5c). In the complete blood count analysis, the white blood cell (WBC) count is 8.41×10^9 L (normal: 5.05-16.76 × 10^9/L), and lymphocyte (Lym) is 2.2 ×10^3/μl (normal: 1.05-5.10 × 10^3/μl). In biochemical analyses, aspartate transaminase (AST) is 52 U/L, which is slightly above the reference range (0–50 U/L), but no evidence of significant liver damage is observed. Total bilirubin (TB), a major indicator of bile duct patency, is 0 mg/dL (normal: 0–0.9 mg/dL), indicating no significant impairment of biliary function during the 1-year implantation period.

After 1-year implantation, the C-SMP exhibits no visible biofilm formation except suture-concentrated growth with barely detectable *E. coli* under SEM (Figure 5d). AFM images reveal clear crystalline alignment with a further reduction of amorphous width compared to those after one and 10 recovery cycle(s). As the surface roughness parameters (R_a and R_q) of SMP increase (Figure S4b), the height difference between crystalline phases (ridges) and amorphous phases (valleys) on the surface becomes more pronounced. These results collectively support the progressive reduction of amorphous spacing as recovery cycles proceed. In addition, the degree of crystallinity increases after 1-year implantation compared to that before insertion, as confirmed by DSC analysis (Figure 5f). These findings indicate that crystalline growth and alignment continue with concomitant reduction of amorphous spacing under in vivo conditions. The causative mechanical stress is generated by body movements, including squeezing actions of bile with involvement of gallbladder contraction, as observed in the canine model of C-SMP tube grafting. In addition,

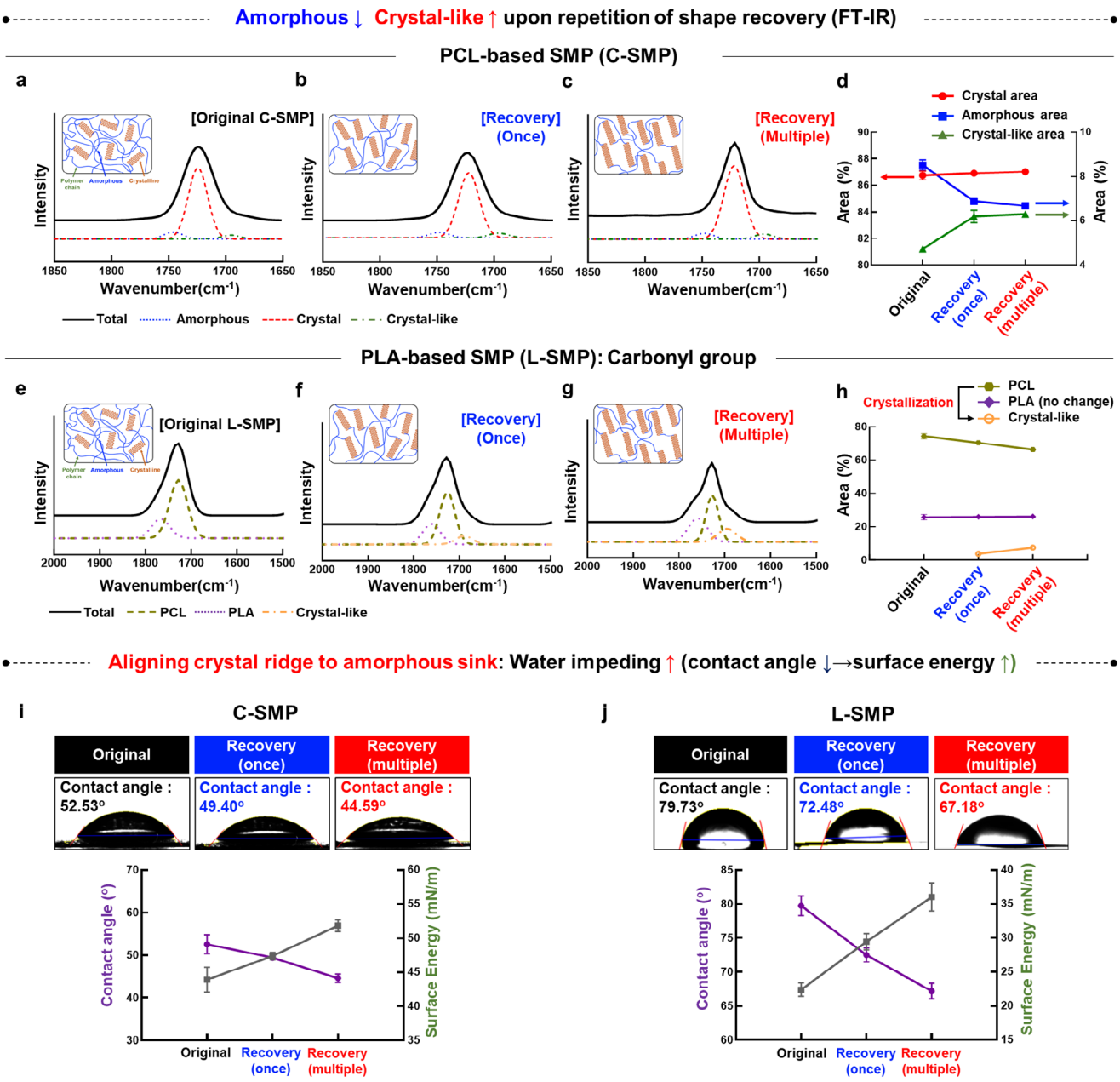

FIGURE 4 | Crystal-like growth to merge and align narrowing amorphous spaces following recovery cycles. Carbonyl stretching is analyzed using FT-IR spectra, and the surface energy is calculated using a water contact angle following recovery cycles (No → Once → Multiple: 10 times). In addition to the black total spectra for both SMP types, the C-SMP peaks are labeled in red (crystal, blue (amorphous), and green (crystal-like), with corresponding comparisons of green (PCL), violet (PLLA), and yellow (crystal-like) for L-SMP. (a–d), C-SMP exhibits new growth of a crystalline-like area (Green peak at 1696 cm^{-1}) with a reduction of the amorphous area (Blue peak at 1723 cm^{-1})and maintenance of the crystalline area (Red peak at 1747 cm^{-1}) in FT-IR. (e–h), The PCL (Green peak at 1720 cm^{-1}) and PLA (Violet peak at 1758 cm^{-1}) components of L-SMP are analyzed using FT-IR spectra. While the PLA area does not change following the recovery cycles, the generation of crystalline-like areas (Yellow peak at 1684 cm^{-1}) increases along with the reduction of the PCL area, indicating recovery-induced crystallization of PCL upon area loss. (i) and (j), Crystalline phases impede water penetration due to tight packing of polymer chains, but ridge formation facilitates water sinking into amorphous grounds upon merging and alignment. This mechanism drives a decrease in the water contact angle along with increases in surface energy following the recovery cycles in both C-SMP and L-SMP. Data = mean ± SD (n = 3).

temperature fluctuation in contact with interstitial flow around the implantation site may serve as another trigger for crystalline growth. In replacing a segment of the canine bile duct, the anti-biofilm effect is maintained for 1 year, which is four times longer than the reported 3-month limit of stent failure. Furthermore, implantation of SMP film subcutaneously in mice for 60 days shows no indication of bacterial infection in H&E images, thereby supporting the canine results (Figure S5).

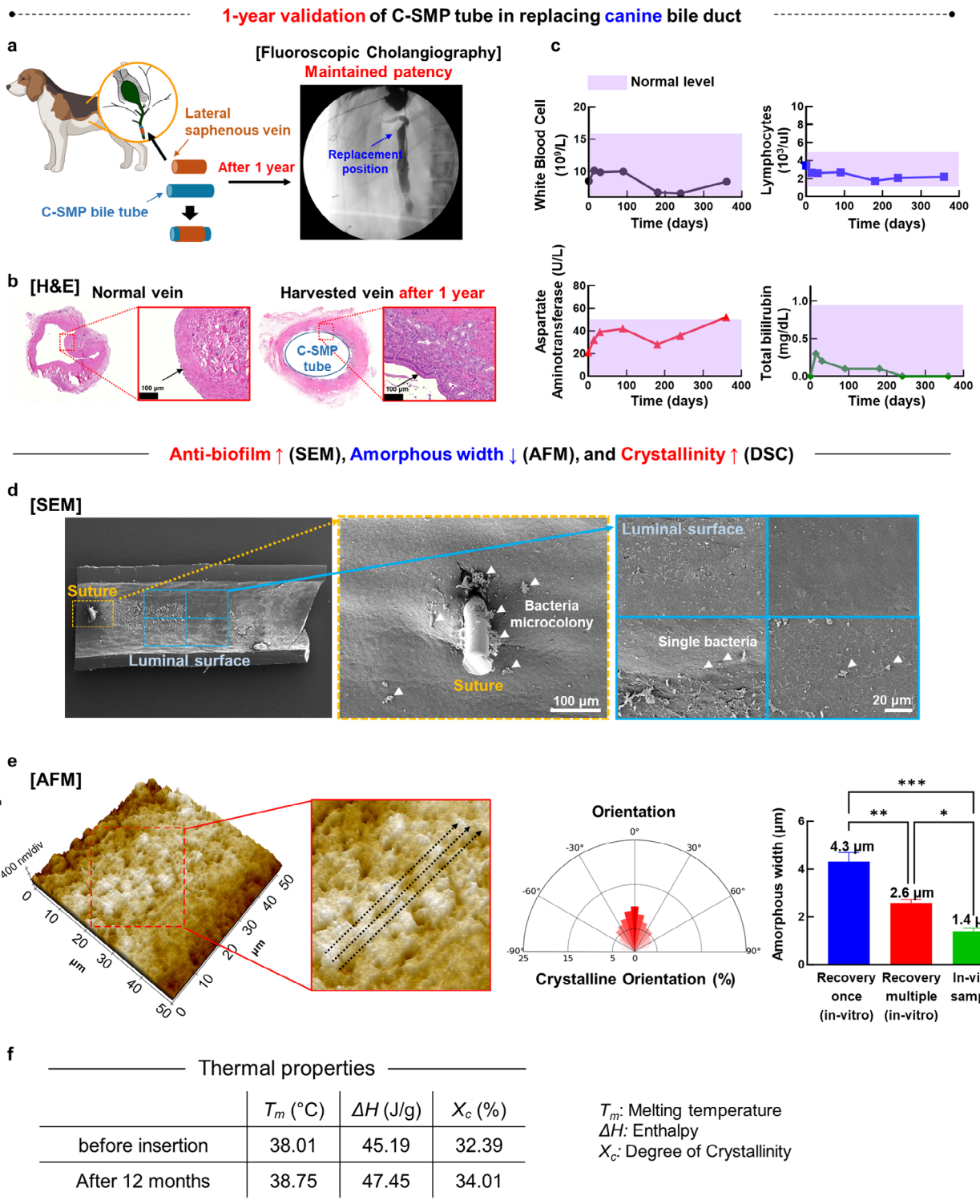

	T_m (°C)	ΔH (J/g)	X_c (%)
before insertion	38.01	45.19	32.39
After 12 months	38.75	47.45	34.01

FIGURE 5 | 1-year validation of in vivo anti-biofilm effect in replacement of canine bile duct. (a), In the beagle dog, a C-SMP tube is wrapped with autologous saphenous vein and used to replace a part of the bile duct. The biliary patency is well maintained for 1 year under fluoroscopic cholangiography (These figures were created with Biorender.com). (b), When the bile duct is harvested after 1 year, the H&E image (right) of the saphenous vein in the replaced position exhibits well-maintained lining cells without any stenotic indication around the surface of the C-SMP tube (sky blue), similar to the normal vein (left). The tube is not seen due to detachment from the vein during the staining process. (c), Blood analysis after 1 year with complete blood counts and biochemistry confirms no infection, with indicators demonstrating proper management of duct function. (d), After 1-year implantation, the luminal surface of the C-SMP tube (sky blue boxes) exhibits only single *E. coli* (white arrows) with no visible biofilm formation, in contrast to the suture area (yellow box), which shows relatively greater microcolony formation (white arrows) under SEM. (e), The in vivo sample shows crystalline alignment with greater reduction of amorphous width than those observed after one and 10 recovery cycles based on AFM analyses. (f), Crystallinity increases after 1-year implantation compared to that before insertion by DSC analysis. Data = mean ± SD (n = 3). *p < 0.05; **p < 0.01; ***p < 0.001 between the lined groups.

3 | Discussion

Most approaches to reduce biofilm formation on medical devices aim to establish surface functions that are expected to be continuously maintained after implantation. However, device surfaces undergo unpredictable alterations upon implantation due to hydration, temperature shifts, erosion, degradation, protein adsorption, inflammation, and cellular remodeling. Once implanted, the environmental parameters change from ambient to intra-body conditions, and the parameters that persist continuously are movement-driven mechanical stress and hydration-driven temperature fluctuation. The present study introduces a valuable concept by leveraging these unavoidable factors to program anti-biofilm functions on device surfaces and to further amplify these effects over time under implantation, particularly under smooth muscle contraction of the bile duct in addition to abdominal movement [72, 73]. The benefit becomes incremental under dynamic inter-body environments such as contraction and flow in the biliary, cardiovascular, or urinary systems. Coating strategies are promising but may be limited when covalent bonding is not generated between device and the coating material due to delamination. Even when covalent bonding is generated between them, surface degradation may become a hurdle in addressing delamination. Although there remains room for further improvement through future studies, the 1-year validation using replacement of a portion of the canine bile duct demonstrates that this approach provides a foundational strategy to utilize the semi-crystalline nature of polymeric devices.

When biofilm formation is examined at high resolution, the initiation step is mediated by interactions between bacteria and polymer surfaces, suggesting that prevention is more feasible and effective than intervention at later stages. Polymers possess unique surface dynamics because their chains can undergo disassembly, packing, and alignment in response to directional forces and temperature changes. Tight packing of polymer chains in crystalline phases increases resistance to water penetration and decreases subsequent protein adsorption, which is a prerequisite for bacterial adhesion. Consequently, bacteria preferentially adhere to amorphous phases, where relatively loose chain packing facilitates protein adsorption. Growth of crystalline phases is inevitably accompanied by a reduction of amorphous phases unless the surface area changes. Moreover, crystalline alignment with growth forms elevated ridges, resulting in merging and alignment of amorphous phases along these ridges. In combination, alignment, growth, and ridge formation reduce amorphous spacing to a size range comparable to that of bacteria, making bacterial adhesion increasingly difficult. Bacteria cannot adhere effectively if focal adhesion cannot be established across the elevated ridges. Even when focal adhesion is initiated, insufficient amorphous spacing limits bacterial spreading required to stabilize adhesion. Although surface roughness parameters obtained from AFM images do not fully elucidate this mechanism, elliptical polarization analysis may help clarify the role of surface topography in future studies, considering mechanisms such as those observed in shark skin for suppression of bacterial adhesion [74–76].

Crystallinity plays a pivotal role in suppressing biofilm formation on SMP surfaces. In contrast to amorphous phases, polymer chains within crystalline phases are tightly packed and aligned, preventing water penetration and protein adsorption. Meanwhile, crystalline ridges facilitate concentration of water contact within amorphous regions, leading to a decrease in water contact angle. As a result, increased surface energy promotes protein adsorption and bacterial adhesion specifically within amorphous spaces. As the programming cycle increases, growth of crystalline ridges increasingly restricts expansion of bacterial colonies consisting of tens to thousands of bacteria within amorphous regions, thereby destabilizing biofilm formation. Upon implantation, polymeric devices experience continuous mechanical stress from bodily and organ movements, as well as temperature fluctuations associated with ambient conditions and inter-body fluid flow. Mechanical stress and temperature fluctuation, particularly under annealing conditions, can induce crystalline changes in semi-crystalline polymers. Because shape programming of SMP devices involves both mechanical deformation and temperature variation, crystalline changes become more pronounced at implantation sites due to synergistic activation by both triggers. In addition, SMPs maintain elastic and crystalline properties across original, temporary, and recovered shapes, enabling gradual phase evolution over time. These characteristics justify the selection of the two SMP types as experimental models in this study.

This study validates that these antibacterial surface dynamics can be instructed by body movement with directional forces and by temperature changes associated with local repetition of hydration and dehydration. Shape memory polymers have unique thermomechanical properties to simulate this instruction from the body because their surface behaviors respond to force and temperature changes in a manner comparable to implanted device surfaces. These phase effects are strengthened upon repetition of programming cycles, similar to long-term implantation in the body. In this regard, the two types of SMPs show promising potential to amplify the anti-biofilm effect during implantation through programmable settings. Moreover, these SMPs provide inherent advantages by enabling minimally invasive temporary shapes before implantation, followed by structural restoration to the original shape after implantation, representing a class of smart materials. The fact that these SMPs undergo shape recovery around body temperature further enhances their clinical applicability.

Further studies are required to examine other types of shape memory polymers, bacterial strains, and animal models beyond the current limitations. In a future study to use large animals (e.g. dogs or pigs), AFM phase imaging in tapping mode would help discern differentiation between crystalline regions (higher modulus) and amorphous regions (lower modulus) more clearly after harvesting SMP samples. In addition, the recovery cycle should be increased until the surface loses its dynamic phase behavior so that the effective duration of property maintenance can be predicted. As a harsh model of biofilm formation, both the number and diversity of animal models should be expanded. The canine experiment began more than one year ago, making it difficult to increase the animal number without prior assurance of long-term model validation. Along the same line, comparisons with appropriate controls, such as pre-programmed SMP tubes and commercial polymeric or metallic stents, would clarify the superiority of biofilm suppression and the protective role of venous wrapping. Notably, C-SMP has been used to produce a nasolacrimal stent that demonstrated successful clinical

outcomes without significant biofilm-related complications in patient studies approved by the Korean FDA. This study therefore provides mechanistic insight into biofilm suppression in patients following deployment of nasolacrimal stents during clinical trials.

4 | Methods

4.1 | Synthesis of Shape Memory Polymer (SMP)

Two types of shape memory polymer (SMP) were synthesized using polycaprolactone (PCL) only and PCL grafted to polylactic acid (PLA), which were abbreviated as C-SMP and L-SMP, respectively. C-SMP was synthesized through a double ring-opening polymerization process involving ϵ-caprolactone (CL) and glycidyl methacrylate (GMA) monomers, as previously reported [43–47]. Briefly, CL (315 mmol), di-pentaerythritol (0.5 mmol), and hydroquinone inhibitor (3.5 mmol, 1:10 molar ratio of hydroquinone to GMA) were reacted at 110 °C for 10 min in a three-necked round bottom flask. Subsequently, GMA (35 mmol) was added to the mixture and stirred for an additional 10 min. Then, 1,5,7-triazabicyclo[4.4.0]dec-5-ene (TBD, 1 mmol) was dissolved in acetonitrile solvent (4 mL) and subjected to a reaction at 110 °C for 6 h under a nitrogen atmosphere. The reaction mixture was cooled to room temperature (25°C) and then dissolved in chloroform (30 mL), leading to the formation of a white precipitate upon introduction into cold diethyl ether (800 mL at 4°C). The final C-SMP product was obtained through vacuum drying at room temperature using OV4-30 dryer (Jeio Tech, Daejeon, Republic of Korea). L-SMP was prepared by grafting PCL to PLA. Briefly, PLA (8 g) and PCL (2 g) were dissolved in xylene (100 mL) and heated at 160°C for 1 hr in a three-necked round bottom flask. Next, benzoyl peroxide inhibitor (0.02 g) was added, followed by stirring for 2 hrs. The mixture was then precipitated in cold methanol. The final L-SMP product was obtained through vacuum drying at room temperature in an OV4-30 dryer (Jeio Tech). PLA was purchased from NatureWorks (Ingeo Biopolymer 4032D, Minnesota, USA), and all other chemicals were obtained from Sigma–Aldrich (St. Louis, MO, USA).

4.2 | SMP Film Preparation With Shape Memory Programing

C-SMP (1 g) was dissolved in N-methyl-2-pyrrolidone (NMP; 1 mL, Sigma–Aldrich) at 37°C, followed by adding 2-hydroxy-1-(4-(hydroxyethoxy)phenyl)-2-methyl-1-propanone (Irgacure 2959; 1mg, Sigma–Aldrich) as a photo-initiator. The solution was poured onto a transparent glass substrate and covered with another transparent glass, followed by UV irradiation (365 nm, 265 mJ cm^{-2}) for 200 s using a UV crosslinker (CL-3000L UV Crosslinker, Analytik Jena, Jena, Germany). The films were vacuum-dried at room temperature for 24 hr to remove residual solvent. L-SMP (1g) was dissolved in chloroform ($CHCl_3$, 20ml, Sigma–Aldrich) and poured into a Teflon Petri dish, followed by drying to remove the solvent.

As a shape-programming process, SMP films underwent i) tensile process by stretching 100%, followed by immersion in hot water at 50 °C (T > T_m, T_g). The samples were ii) immersed in cold water at 4 °C ($T < T_m$, T_g) to fix their temporary shape, iii) followed by placement in warm water (40 °C) to confirm intact shape recovery.

4.3 | Material characterization

Thermal properties were characterized using differential scanning calorimetry (DSC; Discovery DSC25, TA Instruments, Seoul, Republic of Korea). The SMP samples were heated to 150 °C and then cooled to −80 °C in two cycles at 10 °C/min under a nitrogen atmosphere. The DSC thermograms were analyzed to determine melting temperature (T_m), crystallization temperature (T_c), melting enthalpy (ΔH_m), and crystallization enthalpy (ΔH_c). The crystallinity (χ_c, %) was calculated using Equation (1) as follows.

$$\chi_c\,(\%) = \frac{\Delta H_m}{\Delta H_m^\circ} \times 100\% \tag{1}$$

where, ΔH_m° is the 100 % crystalline of PCL (139.5 J/g) or PLA (93.6 J/g).

The crystalline and amorphous structures of the SMP surface were determined using High Resolution-XRD (HR-XRD; Rigaku, Tokyo, Japan) with an X-ray wavelength of 1.5406 Å (Cu Kα) at 40 kV and 40 mA. A broad range of diffraction angles (2θ) from 5° to 30° was examined by maintaining the step time at a rate of 2° min^{-1}. The crystallite size was calculated using the Scherrer Equation (2) as follows.

$$Crystallite\ size\ (nm) = \frac{K\lambda}{\beta cos\theta} \tag{2}$$

where K is the Scherrer constant (K = 0.9); λ is the X-ray wavelength; β is the full width at half maximum (FWHM); and θ is the diffraction angle.

Fourier transform infrared (FTIR) analyses were performed using a Nicolet Summit FTIR spectrometer (Thermo Fisher Scientific, Waltham, United States) by obtaining FTIR spectra at room temperature in a resolution of 2 cm^{-1} with 64 scans for all samples.

The SMP surface was imaged by Field-emission Scanning Electron Microscopy (FE-SEM, JEOL Ltd., Tokyo, Japan) upon sputter-coating with a thin platinum layer by accelerating the voltage to 15 kV.

The sample surface was scanned by Atomic Force Microscopy (AFM, NX-10, Park Systems Corp., Gyeonggi-do, Republic of Korea) in non-contact mode. The AFM tip was raster-scanned over a 50 μm × 50 μm area to obtain height data through generation of a high-resolution topographical map. The average roughness (R_a) and root mean square roughness (R_q) were calculated from multiple independent scans to ensure statistical robustness and to assess surface characteristics relevant to the 2D film structure. R_a and R_q were calculated using Park Systems XEI 5.1.3 software. R_a was defined as the arithmetic mean deviation from the center line and calculated as:

$$R_a = \frac{1}{N}\sum_{i=1}^{N} |\,z_i|$$

and R_q was defined as the root mean square deviation from the center line and calculated as:

$$R_q = \sqrt{\frac{1}{N}\sum_{i=1}^{N} z_i^2}$$

where zi represents the height deviation of each data point from the mean plane and N is the total number of height data points extracted from the AFM scan. The crystalline alignment and amorphous width were determined quantitatively using ImageJ (Fiji, National Institutes of Health, MD, USA). The Orientation J plugin (National Institutes of Health) was used to generate vector field images, thereby providing a visual representation of groove alignment. Further orientation analysis was carried out using the ImageJ Directionality plugin (Fourier components method). Histogram parameters were set to 90 bins across −90° to 90° with 2° of bin spacing. The analysis was performed without applying any threshold-based segmentation or additional filtering, in order to extract histogram data with quantification of orientation angle distribution. The results were further processed in Python to convert orientation frequencies to percentages with visualization using Matplotlib in a theta range of −90° to 90°.

The water contact angle onto the SMP surface was determined using a Phoenix 10 contact angle analyzer (SEO Co., Ltd, Anyang, Republic of Korea) at room temperature. Deionized water (1–2 μl) was dropped to the surface at 25°C, followed by measuring the angle within 30 s. The software of the contact angle meter was used to determine the air phase angle between the water droplet and SMP surface by fitting a tangent line from the droplet boundary to the surface. Patterns were generated on the C-SMP surfaces by pressing or scratching them with sandpaper (100 grit) in addition to glass pressing, which altered the surface roughness without significant changes of crystallinity.

4.4 | In Vitro Study to Culture Bacteria With Crystal Violet and Fluorescence Staining

Escherichia coli (*E. coli*, KCCM 12119; Korean Culture Center of Microorganisms, Seoul, Korea), *Pseudomonas aeruginosa* (*P. aeruginosa*, KCTC 1750; Korean Collection for Type Cultures, Korean Culture Center of Microorganisms), and *Staphylococcus aureus* (*S. aureus*, KCCM 11385; Korean Culture Center of Microorganisms) were cultured in Luria-Bertani (LB) broth (Sigma–Aldrich) at 37 °C until the growth of each bacterial type reached a mid-log phase of growth (optical density of 0.35 at 600 nm). Circular SMP samples (each 3 ea), 4 mm in diameter, were washed three times with Dulbecco's PBS (Welgene, Daegu, Republic of Korea) and used to culture bacteria for 36 h at 37 °C. The samples were stained with 0.1% crystal violet solution for 30 min, followed by three washes with distilled water, air-drying for 60 min, and examination on an inverted optical microscope (Leica DMi8; Leica Microsystems, Wetzlar, Germany). The absorbance values were measured at 600 nm on a microplate reader for quantitative analysis of bacterial adhesion.

Also, bacteria were fluorescently labeled by DNA staining with 5 μM SYTO 9 (green) and 5 μM DAPI (blue) fluorescent dye (Invitrogen, Carlsbad, CA, USA), which were then imaged by confocal laser scanning microscopy (LSM710, Carl Zeiss Microscopy, Oberkochen, Germany) with a 40 × oil immersion objective.

E.coli and fibronectin were labeled with 5 μM DAPI (blue) and 10 μg/mL of fluorescein isothiocyanate (FITC), respectively, and then incubated on C-SMP surfaces under fluorescence microscopy with identification of crystalline spaces by polarized optical microscopy (POM). The overlay of the two microscope techniques enabled discrimination of *E.coli* adhesion and fibronectin adsorption onto amorphous and crystalline spaces of C-SMP with increasing recovery cycles (No → Once → Multiple: 10 times). As a supportive experiment, the total amount of protein adsorbed onto the C-SMP surface and the remaining protein in the culture media supernatant were quantified using a bicinchoninic acid (BCA) assay after incubation with a working solution of fibronectin (0.25 mg/mL) or albumin (Ultra Pure Bovine Serum Albumin; GenDEPOT, Katy, USA; A0100-005; 1 mg/ml) for 4 h at 37 °C.

4.5 | In Vivo Study With a Replacement Model of Canine Bile Duct

The biocompatibility of the SMP was examined through subcutaneous implantation into the dorsal region of mice (BALB/c, 6 weeks, male) for 60 days. All procedures were approved by the Institutional Animal Care and Use Committee of the Yonsei Animal Research Center, University College of Medicine (2019–0205, 2020–0071, and 2021–0048). Each animal was acclimatized to the animal facility for at least 1 week before surgery and anesthetized by intramuscular injection of Zoletil (50 mg kg^{-1}, Virbac Korea, Seoul, Republic of Korea) and xylazine (5mg kg−1, Rompun, Bayer Korea, Seoul, Republic of Korea). Tissue invasion into defects was studied by H&E staining.

Animal application study of SMP biliary stents was approved by the Institutional Animal Care and Use Committee of Chungnam National University (permit number 202304A-CNU-010). A healthy beagle dog (1-year-old, female) was provided by Orient Bio Co., Ltd., (Seongnam, Republic of Korea) and acclimatized to the animal facility for at least 2 weeks before surgery. All procedures were conducted in accordance with established guidelines. All surgical procedures were performed under general anesthesia to minimize pain or discomfort, and humane euthanasia was carried out via intravenous injection of a 10% potassium chloride solution.

A C-SMP tube (outer diameter: 2.0 mm and length: 30 mm) was produced by ultraviolet (UV) curing, and a segment of the saphenous vein with the same dimensions as the tube was harvested from the left hind limb of a Beagle dog. The C-SMP tube was heated above 37 °C and elongated to reduce the diameter to 1.5 mm to facilitate insertion into the vein, followed by cooling to fix the temporary shape. The graft was then immersed in 37 °C saline to induce diameter expansion upon shape recovery. In this manner, the tube was tightly wrapped by the vein and used as a conduit to replace a segment of the canine bile duct for 1 year. After surgical dissection of the bile duct (Figure 5a), the graft was positioned to bridge the defect, and end-to-end anastomosis was performed using 7-0 polydioxanone sutures (PDS II; Ethicon Inc., Raritan, United States) in a simple interrupted pattern. This

technique enabled secure connection and minimized anastomotic tension to maintain bile flow through the graft. Stent migration was prevented by securing the anastomosis between the graft and bile duct using 8-0 polypropylene sutures (Prolene; Ethicon Inc.). The procedure was designed to maintain axial alignment of the graft with the bile duct and to mitigate displacement risks during implantation.

The dog blood was analyzed for complete blood count (CBC) and serum biochemistry until sacrifice. White blood cells (WBC) and lymphocytes (Lym) were quantified using an automatic blood analyzer (ProCyte Dx Hematology Analyzer; IDEXX Laboratories Inc., Westbrook, United States). Liver health and bile patency were evaluated by measuring the levels of aspartate aminotransferase (AST) and total bilirubin (TB), respectively, using a clinical blood chemistry analyzer (Catalyst One Chemistry Analyzer; IDEXX Laboratories Inc.). Fluoroscopic cholangiography (FC) was performed immediately before harvesting the graft (SMP tube-vein) under general anesthesia. C-arm fluoroscopy (BV Pulsera; Philips Medical System, Amsterdam, Netherlands) was conducted in an antegrade manner by injecting a contrast agent (20–30 ml of iohexol, Omnipaque; GE Healthcare, Chicago, United States) through a temporary cholecystostomy with tube insertion into the cystic duct. Hematoxylin and eosin (H&E) staining was applied to the harvested vein after fixation in 10% neutral-buffered formalin in PBS. In addition, the harvested sample was subjected to analyses of morphology by SEM and AFM, as well as thermal properties by DSC, to determine changes in surface properties and crystallinity induced by long-term implantation.

4.6 | Statistical Analysis

All experimental data are expressed as mean ± standard deviation (SD), and the number of samples (n) is indicated in the legend for each figure. One-way analysis of variance (ANOVA) was used for multiple group comparisons, and significance levels were expressed as p values ($^{*}p < 0.05$, $^{**}p < 0.01$, $^{***}p < 0.001$). All statistical analyses were performed using Excel, SigmaPlot (V12.0, Systat Software Inc., San Jose, CA, USA), and GraphPad Prism 9 (GraphPad Software, San Diego, CA, USA). Bacterial fluorescence images were quantitatively analyzed for bacterial counts using COMSTAT software (MathWorks). Quantitative analysis of AFM groove pitch was performed using ImageJ software (Fiji). Three independent experiments were performed, and at least three images were collected for each experiment.

Acknowledgements

This work was supported by a grant of the Korea Health Technology R&D Project through the Korea Health Industry Development Institute (KHIDI), funded by the Ministry of Health & Welfare, Republic of Korea (No. RS-2023-00265566), in addition to a grant of the National Research Foundation of Korea (NRF) funded by the Korea government (MSIT) (No. RS-2023-00302125). The figure illustrations were created using Biorender.com.

Conflicts of Interest

The authors declare no conflicts of interest.

Data Availability Statement

The data that support the findings of this study are available in the supplementary material of this article.

References

1. A. J. Teo, A. Mishra, I. Park, Y.-J. Kim, W.-T. Park, and Y.-J. Yoon, "Polymeric Biomaterials for Medical Implants and Devices," *ACS Biomaterials Science & Engineering* 2, no. 4 (2016): 454–472.

2. D. O. Faigel, "Preventing Biliary Stent Occlusion," *Gastrointestinal Endoscopy* 51, no. 1 (2000): 104–107.

3. J. Yan, Z. Ye, X. Wang, et al., "Recent Research Progresses of Bioengineered Biliary Stents," *Materials Today Bio* 29 (2024): 101290.

4. S. Choudhury, S. Asthana, S. Homer-Vanniasinkam, and K. Chatterjee, "Emerging Trends in Biliary Stents: A Materials and Manufacturing Perspective," *Biomaterials Science* 10, no. 14 (2022): 3716–3729.

5. G. Song, H. Q. Zhao, Q. Liu, and Z. Fan, "A Review on Biodegradable Biliary Stents: Materials and Future trends," *Bioactive Materials* 17 (2022): 488–495.

6. C.-I. Kwon and G. A. Lehman, "Mechanisms of Biliary Plastic Stent Occlusion and Efforts at Prevention," *Clinical Endoscopy* 49, no. 2 (2016): 139–146.

7. B. Jansen, L. P. Goodman, and D. Ruiten, "Bacterial Adherence to Hydrophilic Polymer–Coated Polyurethane Stents," *Gastrointestinal Endoscopy* 39, no. 5 (1993): 670–673.

8. P. Stewart and T. Bjarnsholt, "Risk Factors for Chronic Biofilm-Related Infection Associated With Implanted Medical Devices," *Clinical Microbiology and Infection* 26, no. 8 (2020): 1034–1038.

9. Z. Khatoon, C. D. McTiernan, E. J. Suuronen, T.-F. Mah, and E. I. Alarcon, "Bacterial Biofilm Formation on Implantable Devices and Approaches to Its Treatment and Prevention," *Heliyon* 4, no. 12 (2018): 01067.

10. C. R. Armbruster and M. R. Parsek, "New Insight into the Early Stages of Biofilm Formation," *Proceedings of the National Academy of Sciences* 115, no. 17 (2018): 4317–4319.

11. E. Drenkard and F. M. Ausubel, "Pseudomonas Biofilm Formation and Antibiotic Resistance are Linked to Phenotypic Variation," *Nature* 416, no. 6882 (2002): 740–743.

12. S. Manner, D. M. Goeres, M. Skogman, P. Vuorela, and A. Fallarero, "Prevention of Staphylococcus aureus biofilm formation by antibiotics in 96-Microtiter Well Plates and Drip Flow Reactors: Critical factors influencing outcomes," *Scientific Reports* 7, no. 1 (2017): 43854.

13. G. Cheng, Z. Zhang, S. Chen, J. D. Bryers, and S. Jiang, "Inhibition of Bacterial Adhesion and Biofilm Formation on Zwitterionic Surfaces," *Biomaterials* 28, no. 29 (2007): 4192–4199.

14. G. Feng, Y. Cheng, S.-Y. Wang, D. A. Borca-Tasciuc, R. W. Worobo, and C. I. Moraru, "Bacterial Attachment and Biofilm Formation on Surfaces are Reduced by Small-Diameter Nanoscale Pores: How Small is Small Enough?," *npj Biofilms and Microbiomes* 1, no. 1 (2015): 1–9.

15. L.-C. Xu, Y. Wo, M. E. Meyerhoff, and C. A. Siedlecki, "Inhibition of Bacterial Adhesion and Biofilm Formation by Dual Functional Textured and Nitric Oxide Releasing Surfaces," *Acta Biomaterialia* 51 (2017): 53–65.

16. E. K. Riga, M. Vöhringer, V. T. Widyaya, and K. Lienkamp, "Polymer-Based Surfaces Designed to Reduce Biofilm Formation: From Antimicrobial Polymers to Strategies for Long-Term ApplicationsPolymer-based surfaces designed to reduce biofilm formation: From Antimicrobial polymers to strategies for long-term applications," *Macromolecular Rapid Communications* 38, no. 20 (2017): 1700216.

17. N. Kutner, K. R. Kunduru, L. Rizik, and S. Farah, "Recent Advances for Improving Functionality, Biocompatibility, and Longevity of Implantable Medical Devices and Deliverable Drug Delivery Systems," *Advanced Functional Materials* 31, no. 44 (2021): 2010929.

18. J.-R. Lee, S. W. Yang, C.-I. Kwon, et al., "Anti-Fibrotic and Anti-Stricture Effects of Biodegradable Biliary Stents Braided With Dexamethasone-Impregnated Sheath/Core Structured Monofilaments," *Acta Biomaterialia* 178 (2024): 137–146.

19. B. Shi, H. Wei, H. Miu, et al., "Fabrication of Micro-Porous Polymeric Coating With Dynamic Drug-Eluting Property on Plastic Biliary Stent for Antiproliferative Treatment," *Colloid and Interface Science Communications* 62 (2024): 100801.

20. Y. Li, K. Yuan, C. Deng, et al., "Biliary Stents for Active Materials and Surface Modification: Recent Advances and Future Perspectives," *Bioactive Materials* 42 (2024): 587–612.

21. A. Van Berkel, M. Bruno, J. Bergman, S. Van Deventer, G. Tytgat, and K. Huibregtse, "A Prospective Randomized Study of Hydrophilic Polymer-Coated Polyurethane Versus Polyethylene Stents in Distal Malignant Biliary Obstruction," *Endoscopy* 35, no. 06 (2003): 478–482.

22. Y. Ikada, "Surface Modification of Polymers for Medical Applications," *Biomaterials* 15, no. 10 (1994): 725–736.

23. J. Woo, Y. Na, W. I. Choi, et al., "Functional Ferrocene Polymer Multilayer Coatings for Implantable Medical Devices: Biocompatible, Antifouling, and ROS-Sensitive Controlled Release of Therapeutic drugs," *Acta Biomaterialia* 125 (2021): 242–252.

24. B. Butruk, M. Trzaskowski, and T. Ciach, "Fabrication of Biocompatible Hydrogel Coatings for Implantable Medical Devices Using Fenton-Type Reaction," *Materials Science and Engineering: C* 32, no. 6 (2012): 1601–1609.

25. X. Song, J. Man, X. Zhang, et al., "Fabrication of Robust Zwitterionic Polymer Brushes Based on Surface Wettability Modulation," *Chemical Engineering Journal* 521 (2025): 166551.

26. M. Blachnio, M. Zienkiewicz-Strzalka, J. Kutkowska, and A. Derylo-Marczewska, "Nanosilver–Biopolymer–Silica Composites: Preparation, and Structural and Adsorption Analysis with Evaluation of Antimicrobial Properties," *International Journal of Molecular Sciences* 25, no. 24 (2024): 13548.

27. C. Highmore, G. Melaugh, R. Morris, et al., "Translational Challenges and Opportunities in Biofilm Science: A BRIEF for the Future," *npj Biofilms and Microbiomes* 8, no. 1 (2022): 68.

28. J. Khan, S. M. Tarar, I. Gul, U. Nawaz, and M. Arshad, "Challenges of Antibiotic Resistance Biofilms and Potential Combating Strategies: A Review," *Biotech* 11, no. 4 (2021): 169.

29. A. Ershad-Langroudi, N. Babazadeh, F. Alizadegan, S. M. Mousaei, and G. Moradi, "Polymers for Implantable Devices," *Journal of Industrial and Engineering Chemistry* 137 (2024): 61–86.

30. F. Khan, M. Tanaka, and S. R. Ahmad, "Fabrication of Polymeric Biomaterials: A Strategy for Tissue Engineering and Medical Devices," *Journal of Materials Chemistry B* 3, no. 42 (2015): 8224–8249.

31. M. Ahlhelm, P. Günther, U. Scheithauer, et al., "Innovative and Novel Manufacturing Methods of Ceramics and Metal-Ceramic Composites for Biomedical Applications," *Journal of the European Ceramic Society* 36, no. 12 (2016): 2883–2888.

32. H.-J. Sung, J. Su, J. D. Berglund, B. V. Russ, J. C. Meredith, and Z. S. Galis, "The Use of Temperature–Composition Combinatorial Libraries to Study the Effects of Biodegradable Polymer Blend Surfaces on Vascular Cells," *Biomaterials* 26, no. 22 (2005): 4557–4567.

33. N. Yui, Y. Suzuki, H. Mori, and M. Terano, "Surface Properties of Polypropylene Films As Biomaterials," *Polymer Journal* 27, no. 6 (1995): 614–622.

34. D. Kołbuk, M. Ciechomska, O. Jeznach, and P. Sajkiewicz, "Effect of Crystallinity and Related Surface Properties on Gene Expression of Primary Fibroblasts," *RSC Advances* 12, no. 7 (2022): 4016–4028.

35. I. Firkowska-Boden, X. Zhang, and K. D. Jandt, "Controlling Protein Adsorption Through Nanostructured Polymeric Surfaces," *Advanced Healthcare Materials* 7, no. 1 (2018): 1700995.

36. M. K. Chug and E. J. Brisbois, "Recent Developments in Multifunctional Antimicrobial Surfaces and Applications Toward Advanced Nitric Oxide-Based Biomaterials," *ACS Materials Au* 2, no. 5 (2022): 525–551.

37. M. A. Daeschel and J. McGuire, "Interrelationships Between Protein Surface Adsorption and Bacterial Adhesion," *Biotechnology and Genetic Engineering Reviews* 15, no. 1 (1998): 413–438.

38. D. Cunliffe, C. Smart, C. Alexander, and E. Vulfson, "Bacterial Adhesion at Synthetic Surfaces," *Applied and Environmental Microbiology* 65, no. 11 (1999): 4995–5002.

39. M. Tang, C. Chen, J. Zhu, H. R. Allcock, C. A. Siedlecki, and L.-C. Xu, "Inhibition of Bacterial Adhesion and Biofilm Formation by a Textured Fluorinated Alkoxyphosphazene Surface," *Bioactive Materials* 6, no. 2 (2021): 447–459.

40. M. Behl and A. Lendlein, "Shape-Memory Polymers," *Materials Today* 10, no. 4 (2007): 20–28.

41. A. Lendlein and O. E. Gould, "Reprogrammable Recovery and Actuation Behaviour of Shape-Memory Polymers," *Nature Reviews Materials* 4, no. 2 (2019): 116–133.

42. J. Delaey, P. Dubruel, and S. Van Vlierberghe, "Shape-Memory Polymers for Biomedical ApplicationsShape-Memory Polymers for Biomedical Applications," *Advanced Functional Materials* 30, no. 44 (2020): 1909047.

43. S. W. Lee, J. Carnicelli, D. Getya, I. Gitsov, K. S. Phillips, and D. Ren, "Biofilm Removal by Reversible Shape Recovery of the Substrate," *ACS Applied Materials & Interfaces* 13, no. 15 (2021): 17174–17182.

44. H. Gu, S. W. Lee, S. L. Buffington, J. H. Henderson, and D. Ren, "On-Demand Removal of Bacterial Biofilms Via Shape Memory Activation," *ACS Applied Materials & Interfaces* 8, no. 33 (2016): 21140–21144.

45. Y. C. Shin, J. B. Lee, D. H. Kim, et al., "Development of a Shape-Memory Tube to Prevent Vascular StenosisDevelopment of a Shape-Memory Tube to Prevent Vascular Stenosis," *Advanced Materials* 31, no. 41 (2019): 1904476.

46. J. Y. Park, J. B. Lee, W. B. Shin, et al., "Nasolacrimal Stent With Shape Memory as an Advanced Alternative to Silicone Products," *Acta Biomaterialia* 101 (2020): 273–284.

47. K. Lee, W. Choi, S. Y. Kim, et al., "Laser-Responsive Shape Memory Device to Program the Stepwise Control of Intraocular Pressure in GlaucomaLaser-Responsive Shape Memory Device to Program the Stepwise Control of Intraocular Pressure in Glaucoma," *Advanced Functional Materials* 33, no. 35 (2023): 2300264.

48. H. Ha, C. H. Lee, K. S. Lee, et al., "Shape-Configurable Mesh for Hernia Repair by Synchronizing Anisotropic Body MotionShape-Configurable Mesh for Hernia Repair by Synchronizing Anisotropic Body Motion," *Small* 19, no. 47 (2023): 2303325.

49. S. Cho, K. S. Lee, K. Lee, et al., "Surface Crystal and Degradability of Shape Memory Scaffold Essentialize Osteochondral Regeneration," *Small* 20 (2024): 2401989.

50. S. W. Lee, K. S. Phillips, H. Gu, M. Kazemzadeh-Narbat, and D. Ren, "How Microbes Read the Map: Effects of Implant Topography on Bacterial Adhesion and Biofilm Formation," *Biomaterials* 268 (2021): 120595.

51. K. A. Whitehead, D. Rogers, J. Colligon, C. Wright, and J. Verran, "Use of the Atomic Force Microscope to Determine the Effect of Substratum Surface Topography on the Ease of Bacterial Removal," *Colloids and Surfaces B: Biointerfaces* 51, no. 1 (2006): 44–53.

52. P. Kingshott and H. J. Griesser, "Surfaces that Resist Bioadhesion," *Current Opinion in Solid State and Materials Science* 4, no. 4 (1999): 403–412.

53. B. Rowan, M. A. Wheeler, and R. M. Crooks, "Patterning Bacteria within Hyperbranched Polymer Film Templates," *Langmuir* 18, no. 25 (2002): 9914–9917.

54. M. R. Nejadnik, H. C. van der Mei, W. Norde, and H. J. Busscher, "Bacterial Adhesion and Growth on a Polymer Brush-Coating," *Biomaterials* 29, no. 30 (2008): 4117–4121.

55. A. C. Smith and M. A. Hussey, "Gram Stain Protocols," *American Society for Microbiology* 1, no. 14 (2005): 113–144.

56. K. N. Kragh, M. Alhede, L. Kvich, and T. Bjarnsholt, "Into the Well—A Close Look at the Complex Structures of a Microtiter Biofilm and the Crystal Violet Assay," *Biofilm* 1 (2019): 100006.

57. E. F. Haney, M. J. Trimble, and R. E. Hancock, "Microtiter Plate Assays to Assess Antibiofilm Activity Against Bacteria," *Nature Protocols* 16, no. 5 (2021): 2615–2632.

58. S. Saby, I. Sibille, L. Mathieu, J. Paquin, and J. Block, "Influence of Water Chlorination on the Counting of Bacteria with DAPI (4', 6-Diamidino-2-Phenylindole)," *Applied and Environmental Microbiology* 63, no. 4 (1997): 1564–1569.

59. N. Høiby, T. Bjarnsholt, C. Moser, et al., "ESCMID Guideline for the Diagnosis and Treatment of Biofilm Infections," *Clinical Microbiology and Infection* 21 (2015): S1–S25.

60. R. J. Gaymans, "Segmented Copolymers With Monodisperse Crystallizable Hard Segments: Novel Semi-Crystalline Materials," *Progress in Polymer Science* 36, no. 6 (2011): 713–748.

61. S. Agarwal and C. Speyerer, "Degradable Blends of Semi-Crystalline and Amorphous Branched Poly (Caprolactone): Effect of Microstructure on Blend Properties," *Polymer* 51, no. 5 (2010): 1024–1032.

62. S. Jiang, X. Ji, L. An, and B. Jiang, "Crystallization Behavior of PCL in Hybrid Confined Environment," *Polymer* 42, no. 8 (2001): 3901–3907.

63. X. Wang, H. Zhao, L.-S. Turng, and Q. Li, "Crystalline Morphology of Electrospun Poly (ε-Caprolactone)(PCL) Nanofibers," *Industrial & Engineering Chemistry Research* 52, no. 13 (2013): 4939–4949.

64. K. S. Lee and Y. W. Chang, "Thermal and Mechanical Properties of Poly(ε-Caprolactone)/Polyhedral Oligomeric Silsesquioxane Nanocomposites," *Polymer International* 62, no. 1 (2013): 64–70.

65. T. Watanabe, Y. He, N. Asakawa, N. Yoshie, and Y. Inoue, "Hydrogen-Bonding Interaction Between Poly(ε-Caprolactone) and Low-Molecular-Weight Amino Compounds," *Polymer International* 50, no. 4 (2001): 463–468.

66. Y. He and Y. Inoue, "Novel FTIR Method for Determining the Crystallinity of Poly(?-Caprolactone)," *Polymer International* 49, no. 6 (2000): 623–626.

67. M.-H. Huang, S. Li, and M. Vert, "Synthesis and Degradation of PLA–PCL–PLA Triblock Copolymer Prepared by Successive Polymerization of ε-Caprolactone and dl-Lactide," *Polymer* 45, no. 26 (2004): 8675–8681.

68. K. Garkhal, S. Verma, S. Jonnalagadda, and N. Kumar, "Fast Degradable Poly(L -Lactide- co -ε-Caprolactone) Microspheres for Tissue Engineering: Synthesis, Characterization, and degradation Behavior," *Journal of Polymer Science Part A: Polymer Chemistry* 45, no. 13 (2007): 2755–2764.

69. K. S. Kim, C. M. Ryu, C. S. Park, G. S. Sur, and C. E. Park, "Investigation of Crystallinity Effects on the Surface of Oxygen Plasma Treated Low Density Polyethylene Using X-Ray Photoelectron Spectroscopy," *Polymer* 44, no. 20 (2003): 6287–6295.

70. J.-H. Oh, M.-W. Moon, and C. H. Park, "Effect of Crystallinity on the Recovery Rate of Superhydrophobicity in Plasma-Nanostructured Polymers," *RSC Advances* 10, no. 18 (2020): 10939–10948.

71. K. Guo, S. Freguia, P. G. Dennis, et al., "Effects of Surface Charge and Hydrophobicity on Anodic Biofilm Formation, Community Composition, And Current Generation in Bioelectrochemical Systems," *Environmental Science & Technology* 47, no. 13 (2013): 7563–7570.

72. S.-M. Hong, G. H. Kang, H. Y. Lee, and J. Y. Ro, "Smooth Muscle Distribution in the Extrahepatic Bile Duct: Histologic and Immunohistochemical Studies of 122 Cases," *The American Journal of Surgical Pathology* 24, no. 5 (2000): 660–667.

73. M. Strazzabosco and L. Fabris, "Functional Anatomy of Normal Bile Ducts," *The Anatomical Record: Advances in Integrative Anatomy and Evolutionary Biology* 291, no. 6 (2008): 653–660.

74. H.-W. Chien, X.-Y. Chen, W.-P. Tsai, and M. Lee, "Inhibition of Biofilm Formation by Rough Shark Skin-Patterned Surfaces," *Colloids and Surfaces B: Biointerfaces* 186 (2020): 110738.

75. A. Sakamoto, Y. Terui, C. Horie, et al., "Antibacterial Effects of Protruding and Recessed Shark Skin Micropatterned Surfaces of Polyacrylate Plate With a Shallow Groove," *FEMS Microbiology Letters* 361, no. 1 (2014): 10–16.

76. L.-C. Pan, S.-Y. Hsieh, W.-C. Chen, et al., "Self-Assembly of Shark Scale-Patterned Tunable Superhydrophobic/Antifouling Structures With Visual Color Response," *ACS Applied Materials & Interfaces* 15, no. 29 (2023): 35311–35320.

Supporting Information

Additional supporting information can be found online in the Supporting Information section.

Supporting File 1: smll73080-sup-0001-SuppMat.docx.

Supporting File 2: smll73080-sup-0002-MovieS1.mov.

Supporting File 3: smll73080-sup-0003-MovieS2.mov.

Supporting File 4: smll73080-sup-0004-MovieS3.mov.

Supporting File 5: smll73080-sup-0005-MovieS4.mov.